Advanced Energy Materials

ADVANCED ENERGY MATERIALS
www.advenergymat.de

RESEARCH ARTICLE

Atomically Tandem F and P Dual-Doped Co Catalyst Triggers NO_2 Spillover for Enhanced Ammonia Electrosynthesis from Dilute Nitrate

Jia Ran[1] | Keqing Fang[1] | Yu-Lin Sun[2] | Xinzai Lv[1] | Haiyan Wang[1] | Xiaolin Feng[1] | Rihui Li[1] | Fang Chen[3] | Zhongqing Ma[4] | Yong Hu[2]

[1]Department of Chemistry, Key Laboratory of the Ministry of Education for Advanced Catalysis Materials, Zhejiang Normal University, Jinhua, China | [2]Institute of Nanocatalysis and Energy Conversion, College of Chemistry and Materials Engineering, Zhejiang A&F University, Hangzhou, China | [3]Hangzhou Institute of Advanced Studies, Zhejiang Normal University, Hangzhou, China | [4]Bamboo Industry Institute, Zhejiang A & F University, Hangzhou, Zhejiang, China

Correspondence: Haiyan Wang (chemwhy@zjnu.edu.cn) | Fang Chen (chenfang@zjnu.edu.cn) | Zhongqing Ma (mazq@zafu.edu.cn) | Yong Hu (yonghu@zafu.edu.cn; yonghu@zjnu.edu.cn)

Received: 12 September 2025 | **Revised:** 1 November 2025 | **Accepted:** 13 November 2025

Keywords: dilute nitrate | electrochemical nitrate reduction to ammonia | F and P co-doped Co | NO_2 Spillover | tandem electrocatalysts

ABSTRACT

Electrochemical nitrate reduction to ammonia (NO_3RR) represents a promising strategy for sustainable NH_3 synthesis and environmental remediation. However, it is critically challenged by high overpotentials and the hydrogen evolution reaction, especially in dilute nitrate environments. Herein, we report an atomically precise tandem electrocatalyst with fluorine and phosphorus dual-doped cobalt (F, P-Co) that achieves a record-high NH_3 yield rate of 357.5 μmol h^{-1} cm^{-2} with 96.0% Faradaic efficiency at a low potential of −0.5 V vs. RHE. It exhibits exceptional stability for over 200 h in a 10 mM NO_3^- solution, ranking it among the best-performing catalysts for low-concentration NO_3RR. Notably, in a biomass-coupled flow cell, it attains a high current density of 200 mA cm^{-2}, demonstrating great promise for practical application. Mechanistic studies unveil that the F and P co-doping synergistically alters the potential-determining step and lowers the reaction barrier via an atomic relay mechanism involving $*NO_2$ spillover. Specifically, F-Co sites facilitate the adsorption and reduction of NO_3^- to $*NO_2$, whereupon the generated $*NO_2$ intermediate spontaneously migrates to adjacent P-Co sites for subsequent hydrogenation. This work provides a fundamental principle for designing efficient tandem catalysts and establishes a viable pathway for energy-efficient ammonia electrosynthesis.

1 | Introduction

The global nitrogen balance has been profoundly disrupted by the extensive use of nitrogen fertilizers in industry and agriculture [1, 2]. This practice has led to widespread nitrate (NO_3^-) pollution in surface and groundwater, a pervasive environmental problem that exacerbates eutrophication and poses significant risks to human health [3, 4]. The conversion of waste NO_3^- into ammonia (NH_3), an essential feedstock for fertilizers and a potential carbon-free energy carrier, presents a promising strategy for environmental and economic sustainability [5]. The production of NH_3, however, is currently dominated by the energy-intensive Haber-Bosch process, which consumes approximately 2% of the world's energy supply and is responsible for 1%–2% of global

J.R. and K.F. contributed equally to this work.

carbon dioxide emissions [6–9]. In light of these challenges, the electrochemical reduction of NO_3^- (NO_3RR) has emerged as an energy-efficient and sustainable alternative for NH_3 synthesis under ambient conditions [10–13].

The electrochemical conversion of NO_3^- to NH_3 is a complex process involving a nine-proton, eight-electron transfer, which is hindered by sluggish kinetics and poses a significant challenge for catalyst design [14–18]. Despite notable advancements in NO_3RR, most reported breakthroughs have been confined to high NO_3^- concentrations (≥100 mM) in strongly acidic or alkaline electrolytes [19–25]. In practice, however, the NO_3^- concentration in industrial and agricultural wastewater is typically much lower (eg, <1500 ppm) [26–28]. Under such dilute conditions, the NH_3 production efficiency is severely constrained by two fundamental challenges: intensified competition from the hydrogen evolution reaction (HER) and scaling relationships among multiple intermediates [26, 29]. Furthermore, while extreme pH conditions have been demonstrated to enhance hydrogenation kinetics, they often reduce equipment longevity and electrocatalyst stability [30–32]. It is therefore imperative to develop efficient and durable electrocatalysts for the electrocatalytic reduction of nitrate in neutral and low-concentration environments.

The concept of mimicking nature has emerged as a promising strategy for optimizing multi-step electrochemical reactions [33–37]. In biological systems, the enzymatic reduction of NO_3^- to NH_3 follows a cascade mechanism: nitrate reductases first catalyze the two-electron reduction of NO_3^- to NO_2^-, and then nitrite reductases convert NO_2^- to NH_3 [38–40]. Inspired by this principle, recent studies have developed tandem electrocatalysts that circumvent scaling relationships and overcome high reaction barriers in the NO_3RR, thereby improving NH_3 synthesis efficiency [41–44]. For instance, He et al. developed a potential-dependent tandem catalyst featuring a Cu/CuO_x core for NO_3^--to-NO_2^- reduction and a Co/CoO shell for subsequent NO_2^--to-NH_3 conversion [45]. Similarly, Liu et al. demonstrated tandem catalysis using a Co_3O_4/single-atom Cu heterostructure [46]. However, conventional tandem catalysts with spatially separated active species inevitably face limitations due to slow desorption and diffusion of intermediates, which hinder efficient transfer and promote the formation of unwanted by-products.

In this work, we designed an atomically tandem catalyst through dual doping of fluorine and phosphorus into cobalt (denoted as F, P-Co) to facilitate intermediate migration and promote the electroreduction of dilute NO_3^- to NH_3. Experiments and theoretical computations collectively reveal that the synergistic effect of F and P dual-doping enhances NO_3^- adsorption, accelerates hydrogenation kinetics, and lowers the reaction energy barrier, thereby significantly boosting the NO_3RR performance. Crucially, an atomic relay mechanism mediated by $*NO_2$ spillover was elucidated: F-Co sites preferentially adsorb and reduce NO_3^- to $*NO_2$, after which the generated $*NO_2$ intermediates spontaneously migrate to adjacent P-Co sites for efficient hydrogenation. This inner cascade catalysis endows the F, P-Co catalyst with exceptional performance, achieving a record-high NH_3 yield rate (Y_{NH3}) of 357.5 μmol h^{-1} cm^{-2} with a Faradaic efficiency (FE_{NH3}) of 96.0% at a low potential of –0.5 V vs. reversible hydrogen electrode (RHE). The catalyst also demonstrates remarkable stability for 200 h in a neutral 10 mM NO_3^- solution, ranking it among the best-performing catalysts for low-concentration NO_3RR in neutral media. Furthermore, a high NH_3 yield rate of 889.5 μmol h^{-1} cm^{-2} was achieved at a large current density of 200 mA cm^{-2} within a 5-hydroxymethylfurfural (HMF)-coupled flow cell, underscoring its significant potential for scalable and economically viable NH_3 production.

2 | Results and Discussion

The F, P-Co catalyst was synthesized on copper foam (CF) via a simple one-step electrodeposition method with $CoSO_4$, $NaH_2PO_2{\cdot}H_2O$, and NH_4F as the cobalt, phosphorus, and fluorine precursors, respectively (Figure 1a). Field emission scanning electron microscopy (FESEM) images show a rough-textured coating on the CF substrate (Figure S1). The transmission electron microscopy (TEM) image further reveals a porous architecture of the catalyst (Figure 1b), and the high-resolution TEM (HRTEM) image shows distinct lattice fringes with an interplanar spacing of 0.217 nm, corresponding to the (100) plane of hexagonal Co (Figure 1c). Abundant structural defects observed in the F, P-Co catalyst is expected to serve as additional active sites. Furthermore, the selected area electron diffraction (SAED) pattern verifies the metallic Co phase, as evidenced by diffraction rings corresponding to the (002), (110), and (103) planes (Figure S2). Energy dispersive X-ray spectroscopy (EDX) mapping further validates the homogeneous distribution of Co, F and P elements throughout the catalyst, verifying successful dual doping of F and P (Figure S3). The doping amounts of F and P in F, P-Co, as determined by ion chromatography, are 2.7 and 1.8 wt.%, respectively. To facilitate comparison, control samples including P-doped Co (P-Co), F-doped Co (F-Co) and pure Co catalysts were prepared under identical conditions by selecting respective doping precursors (Figure S4). Powder X-ray powder diffraction (XRD) was further carried out to determine the phase composition of the catalysts. As shown in Figure 1d, all samples exhibit diffraction peaks corresponding to hexagonal metallic Co (JCPDS No. 05-0727), with no detectable impurities. Notably, the broader diffraction peaks observed for the F,P-Co catalyst indicate lower crystallinity, which may be attributed to the dual-doping of F and P. Furthermore, Raman spectroscopy shows no obvious signals for CoF or CoP compounds, confirming that F and P are incorporated as dopants rather than forming distinct phases (Figure S5). Collectively, these results consistently verify that the F, P-Co catalyst is primarily composed of metallic Co with F and P incorporated as dopants.

The surface elemental composition and chemical states of the catalysts were probed by X-ray photoelectron spectroscopy (XPS). The survey spectrum confirms the coexistence of Co, F, and P elements in the F, P-Co catalyst (Figure S6a). High-resolution Co 2*p* XPS analysis reveals two characteristic spin-orbit doublets, corresponding to Co^{2+} (781.2/797.1 eV) and Co^0 (778.25/793.3 eV), accompanied by satellite peaks (Figure 1e) [47]. The presence of Co^{2+} species in the pure Co catalyst is attributed to surface oxidation in air [48]. Notably, the ratio of Co^{2+}/Co^0 in the F, P-Co catalyst is approximately 1.0, which lies between the values observed for F-Co (3.9) and P-Co (0.90) (Table S1). This trend clearly reflects the complementary electronic effects of F (electron acceptor) and P (electron donor) in modulating the

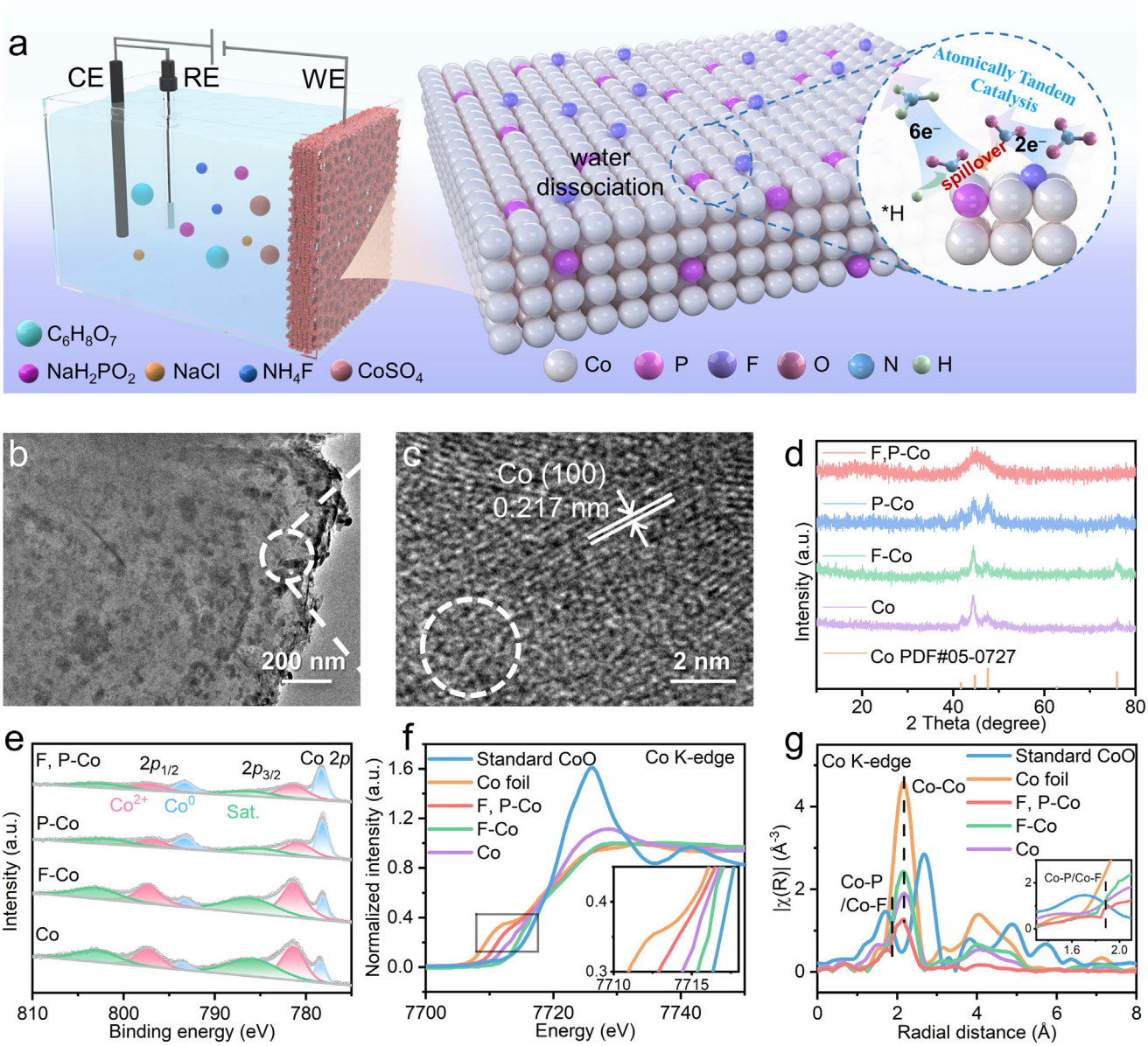

FIGURE 1 | Preparation and characterization of F, P-Co. a) Schematic illustration of the synthetic process of F, P-Co. b) TEM image and c) HRTEM image of F, P-Co. d) XRD patterns of the F, P-Co, P-Co, F-Co and Co catalysts. e) High-resolution Co 2p XPS spectra. f) Normalized Co K-edge XANES spectra and g) FT-EXAFS spectra of F, P-Co, F-Co, Co and the standard CoO and Co foil.

electronic structure of Co. The P 2*p* spectra display two high-resolution peaks of P $2p_{3/2}$ and P $2p_{1/2}$ at 129.1 and 130.0 eV, respectively, which are both assigned to the Co—P bonds, along with P—O species (132.5 eV) from surface oxidation (Figure S6b) [49]. Furthermore, the high-resolution F 1*s* spectra confirm the formation of Co—F bonds, providing evidence for the successful incorporation of F atoms in F, P-Co and F-Co (Figure S6c) [50]. To gain further insight into the local coordination environment, X-ray absorption spectroscopy (XAS) was performed. As illustrated in the Co K-edge X-ray absorption near-edge structure (XANES) spectra, the absorption edge of F, P-Co shift slightly to lower energy compared to F-Co and pure Co, indicating a reduced average oxidation state of Co (Figure 1f). In the Fourier transformed extended X-ray absorption fine structure (FT-EXAFS) spectra, two prominent peaks are observed at 1.88 and 2.20 Å, corresponding to the Co—P/F and Co—Co coordination shells. This provides direct evidence for the formation of the F, P-Co catalyst (Figure 1g) [51, 52].

The electrocatalytic nitrate reduction performance of F, P-Co was evaluated in a standard three-electrode H-cell containing 10 mM KNO_3 in 0.1 M K_2SO_4 electrolytes under ambient conditions. All potentials were referenced against the RHE without *iR* compensation. Linear sweep voltammetry (LSV) profiles reveal a remarkable increase in the current density upon the addition of NO_3^- for all catalysts, signifying their electrocatalytic NO_3RR activity (Figure S7). The LSV profile of the F, P-Co catalyst in nitrate-containing electrolyte exhibits three distinct regions, corresponding to the sequential conversions of NO_3^--to-NO_2^-, NO_2^--to-NH_3, and H_2O-to-H_2 [43, 53, 54]. This three-region profile suggests an efficient two-step relay mechanism for the NO_3RR. In contrast, the control samples (F-Co, P-Co and pure

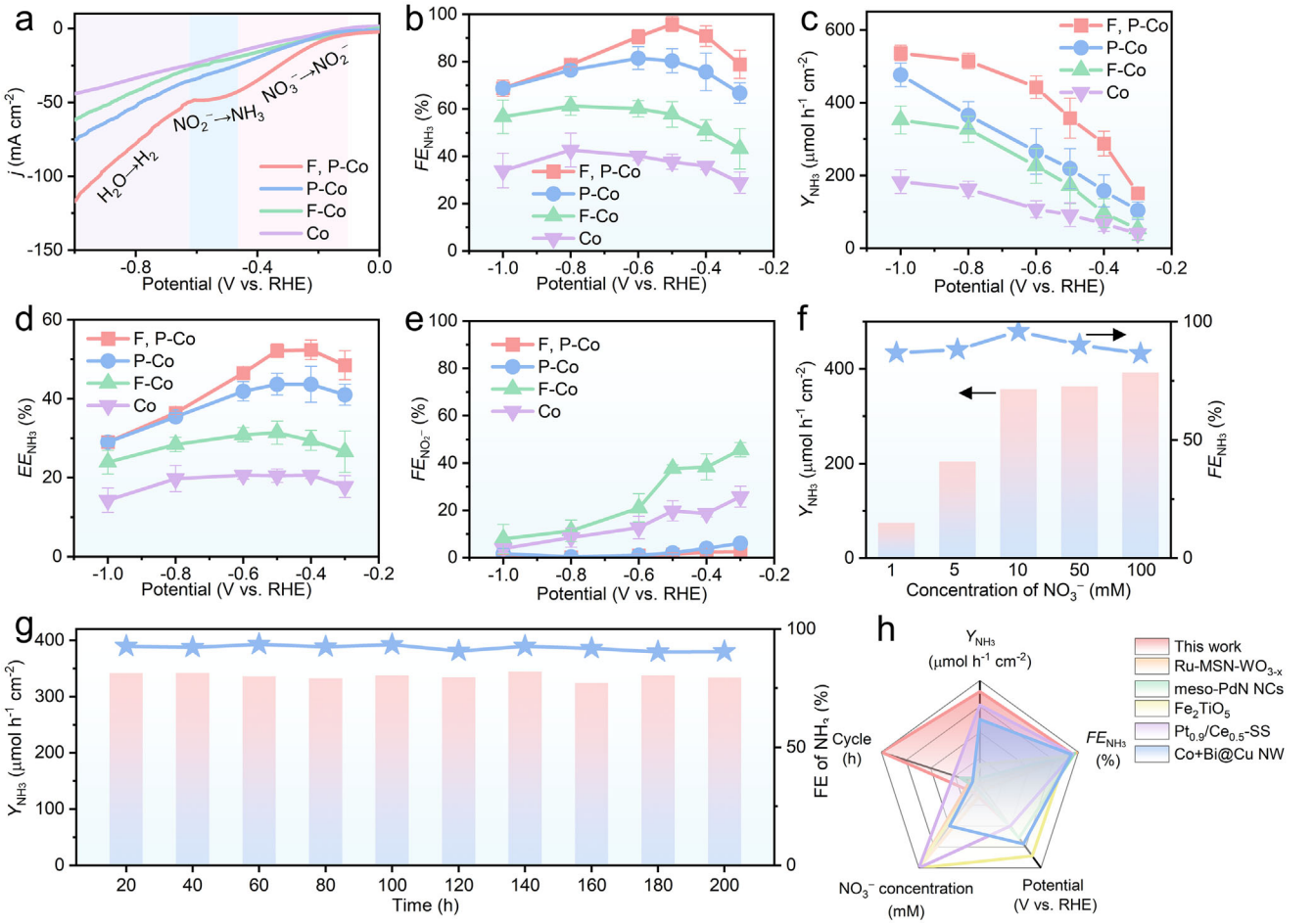

FIGURE 2 | Electrocatalytic NO_3RR performance toward ammonia. a) LSV curves of F, P-Co, P-Co, F-Co and Co in 0.1 M K_2SO_4 + 10 mM KNO_3 electrolytes at 10 mV s^{-1}. b) FE_{NH3}, c) Y_{NH3}, d) EE_{NH3}, and e) FE_{NO2}^- of F, P-Co, P-Co, F-Co and Co at different potentials. f) Y_{NH3} and FE_{NH3} of F, P-Co at −0.5 V vs. RHE in various concentrations of NO_3^- from 1 to 100 mM. g) Electrocatalytic stability of F, P-Co in a flow cell at −0.5 V vs. RHE. h) Comparisons of Y_{NH3}, FE_{NH3}, cycle, optimal potential and NO_3^- concentration for the F, P-Co catalyst with the state-of-the-art electrocatalysts in neutral electrolytes.

Co) display only two regions, further affirming the critical role of F, P dual-doping in establishing this altered reaction pathway. Furthermore, the F, P-Co catalyst achieves the highest current density among all samples, indicating superior NO_3RR activity (Figure 2a). This enhanced performance is corroborated by Tafel analysis, where F, P-Co shows the lowest Tafel slope (67.5 mV dec^{-1}), suggesting the most favorable reaction kinetics (Figure S8).

Chronoamperometry measurements at various potentials were further performed to evaluate the NH_3 electrosynthesis performance (Figure S9). The concentrations of NO_3^-, NO_2^-, and NH_4^+ were quantified by UV–vis spectroscopy (Figures S10–S12). As illustrated, the FE_{NH3} on F, P-Co manifests a volcano-shaped dependence on potential, reaching a maximum of 96.0% at a relatively low potential of −0.5 V vs. RHE with a corresponding Y_{NH3} of 357.5 μmol h^{-1} cm^{-2} (Figure 2b,c). These results surpass the values for the comparisons. Additionally, Y_{NH3} of F, P-Co reaches 536.7 μmol h^{-1} cm^{-2} at −1.0 V vs. RHE, superior to those of the F-Co, P-Co and Co catalysts. Nevertheless, the FE_{NH3} of F, P-Co declines as the potential increases, due to intensified competition from the HER. Remarkably, the F, P-Co catalyst achieves a high half-cell energy efficiency for NH_3 (EE_{NH3}) of 52.1% at −0.5 V vs. RHE, indicating the improved energy utilization (Figure 2d). The superior activity of F, P-Co is also proved by the larger partial current densities for NH_3 (j_{NH3}) across all potentials (Figure S13). To elucidate the distinct roles of F and P doping, we compared the FEs for NO_2^- (FE_{NO2}^-) of the four catalysts (Figure 2e). F-Co generates a higher FE_{NO2}^- than the other samples, indicating that F doping promotes the conversion of NO_3^- to NO_2^-. However, the subsequent hydrogenation of $*NO_2^-$ to NH_3 is sluggish on F-Co, probably due to weak $*NO_2^-$ adsorption and limited active hydrogen (*H) availability. In contrast, P incorporation enhances NO_2^- conversion, as evidenced by the minimal NO_2^- byproducts for P-Co and F, P-Co. Notably, the lowest FE_{NO2}^- was obtained for F, P-Co, underscoring the synergetic role of F and P co-doping in promoting NH_3 synthesis. These findings confirm that F-doping facilitates NO_3^- to NO_2^- conversion, while P-doping promotes NO_2^- reduction to NH_3, collectively enabling an efficient tandem process on the F, P–Co catalyst.

The influence of nitrate concentration (1–100 mM NO_3^-) on ammonia electrosynthesis was systematically examined. As illustrated, the FE_{NH3} of F, P-Co always maintains above 80% at −0.5 V vs. RHE across the concentration range, suggesting exceptional adaptability to varying NO_3^- concentrations (Figure 2f).

Furthermore, the stability of F, P-Co was evaluated in flow cells by consecutive chronoamperometry tests at −0.5 V vs. RHE. Impressively, during the long-term consecutive electrolysis for 200 h, no significant degradation in the current density is observed, and the FE_{NH3} and Y_{NH3} remain relatively stable (Figure 2g; Figure S14). In addition, post-characterizations by FESEM and XRD confirm the structural stability of F, P-Co, with negligible morphological or phase changes after long-term testing (Figure S15). The Y_{NH3}, FE_{NH3}, cycle, the optimal potential, and NO_3^- solution for NH_3 electrosynthesis are also comparable or even superior to the state-of-the-art electrocatalysts in neutral dilute electrolytes, highlighting the outstanding performance of F, P-Co for neutral NO_3RR in dilute solutions (Figure 2h; Tables S2 and S3) [32, 55–58].

To validate the distinct advantage of F, P-Co, the intrinsic activity of the catalysts was estimated by normalizing LSV curves with the electrochemically active surface area. The electrochemically active surface area can be evaluated by electrochemical double-layer capacitance (C_{dl}) based on cyclic voltammetry (CV) curves. As shown in Figure S16, the F, P-Co delivers the largest C_{dl}, followed by P-Co and F-Co, with pure Co showing the lowest capacitance, which illustrates that the F, P-Co can provide more active sites for NO_3RR. Importantly, the C_{dl}-normalized current densities of F, P-Co remain higher than those of the control samples, confirming its superior intrinsic activity toward NO_3RR (Figure S17). To verify the origin of the produced NH_3, control experiments were conducted at −0.5 V in NO_3^--free solution and at open-circuit potential. Negligible NH_3 was detected in both cases, confirming that the NH_3 is produced exclusively from the electroreduction of NO_3^- and not from catalyst decomposition (Figure S18). In addition, ^1H nuclear magnetic resonance (NMR) spectra cooperated with isotope labeling experiments show typical double or triple peaks in 10 mM $^{15}NO_3^-$ or $^{14}NO_3^-$, respectively, matching well with those of the $^{14}NH_4^+$ and $^{15}NH_4^+$ standards (Figure S19). These findings provide unambiguous evidence that the produced NH_3 certainly comes from NO_3RR [59, 60]. Moreover, when a bare CF substrate was used as the working electrode, only trace NH_3 was detected, further elucidating the essential role of F, P-Co in NO_3RR (Figure S20).

The efficiency of F, P-Co catalyst for NO_3^- removal was evaluated by consecutive chronoamperometry at −0.5 V in a 10 mM NO_3^- solution. As illustrated in Figure S21, almost all NO_3^- are converted to NH_3 within 3 h with a removal efficiency of 97.8%. The concentrations of NO_3^- and NO_2^- after electrocatalysis are both below the World Health Organization (WHO) standards for drinking water. Furthermore, considering the complexity of actual wastewater and the possible impact of interfering ions, we investigated the electrocatalytic performance of F, P-Co in simulated wastewater containing common interfering species, including chemical oxygen demand (COD), Cl^-, PO_4^{3-}, CO_3^{2-}, Ca^{2+}, Mg^{2+}, Fe^{3+}, Mn^{2+}, and Zn^{2+} ions in 10 mM NO_3^- solutions (Figure S22). As shown, the NO_3RR performance of the F, P-Co catalyst remained largely unaffected by these interfering ions, validating its significant potential in practical wastewater treatment.

Furthermore, the charge transfer kinetics at the electrode/electrolyte interface of the F, P-Co catalyst were probed by electrochemical impedance spectroscopy (EIS) at −0.5 V vs. RHE. As shown in Figure S23, F, P-Co exhibits the fastest reaction kinetics, with the lowest charge transfer resistance (R_{ct}) of 12.97 Ω. Additionally, bode phase plots were adopted to analyze the dynamic performance of *H generation and consumption over the different catalysts. As a competing reaction to NO_3RR, the HER involves two key processes: the Volmer step (water dissociation to form *H) and the Heyrovsky step (*H consumption), which typically take place in the low-frequency and mid-frequency regions in Bode plots, respectively [61]. Notably, the phase angles of Co and F-Co appear in the low-frequency region, manifesting that the dynamic equilibrium is primarily dominated by the Volmer step (Figure 3a). In contrast, the peak position in the Bode curve shifts to a higher frequency after P doping, indicating that the dynamic equilibrium of water dissociation is perturbed due to the enhanced *H generation capability and effective *H capture by NO_X intermediates. Strikingly, the F, P-Co displays the highest frequency shift and the lowest intensity among the four catalysts, suggesting that F and P co-doping synergistically promote water dissociation and facilitate efficient H* utilization in NO_3RR. Furthermore, *operando* EIS was conducted to probe the potential-dependent electrocatalytic dynamics. As depicted, the R_{ct} values for F, P-Co, P-Co, F-Co, and Co decrease progressively with increasing applied potential, reflecting the accelerated reaction rates (Figure 3b,c; Figure S24). Significantly, the F, P-Co consistently delivers the smallest R_{ct} when the potential ranges from −0.3 to −1 V vs. RHE, corroborating its better electrocatalytic performance. These findings align with the Bode plot analysis, where the F, P-Co demonstrates reduced peak intensities (Figure 3d; Figure S25). The rapid reaction kinetics of F, P-Co were further validated by activation energy (E_a) measurements. As expected, the F, P-Co exhibits an E_a of 21.03 kJ mol^{-1}, significantly lower than those of P-Co (26.76 kJ mol^{-1}), F-Co (27.48 kJ mol^{-1}) and Co (27.56 kJ mol^{-1}), further validating its enhanced activity toward NO_3RR (Figure 3e; Figure S26).

To clarify the origin for the discrepancy, the respective roles of F and P doping on the reaction kinetics of the consecutive NO_3^--to-NO_2^- and NO_2^--to-NH_3 pathways were explored. Figure 3f compares the potentials required for the four catalysts to achieve −5 mA cm^{-2} in 10 mM NO_3^- and NO_2^- solutions. As shown, the F, P-Co and F-Co manifest relatively more positive potentials in NO_3^- solution in comparison to P-Co and Co, suggesting that F doping facilitates NO_3^- adsorption and reduction. Nevertheless, for the NO_2^--to-NH_3 step, F, P-Co and P-Co require significantly lower potentials, elucidating that P doping favors the subsequent deoxidation and hydrogenation of NO_2^-. Importantly, the F, P-Co needs the lowest potentials in both 10 mM NO_3^- and NO_2^- solutions, highlighting its supreme activity toward NO_3RR. These results demonstrate that the F, P-Co catalyst synergistically combines the advantages of individual F and P doping, thereby promoting the stepwise transformation of NO_3^- to NH_3.

Afterward, to verify the cascade mechanism, the reaction rate constants for the NO_3^--to-NO_2^- (k_1) and NO_2^--to-NH_3 (k_2) reduction steps were calculated (Figure 3g). The larger k_1 values for F, P-Co and F-Co relative to P-Co and pure Co confirm that F doping accelerates the initial reduction of NO_3^- to NO_2^-. In

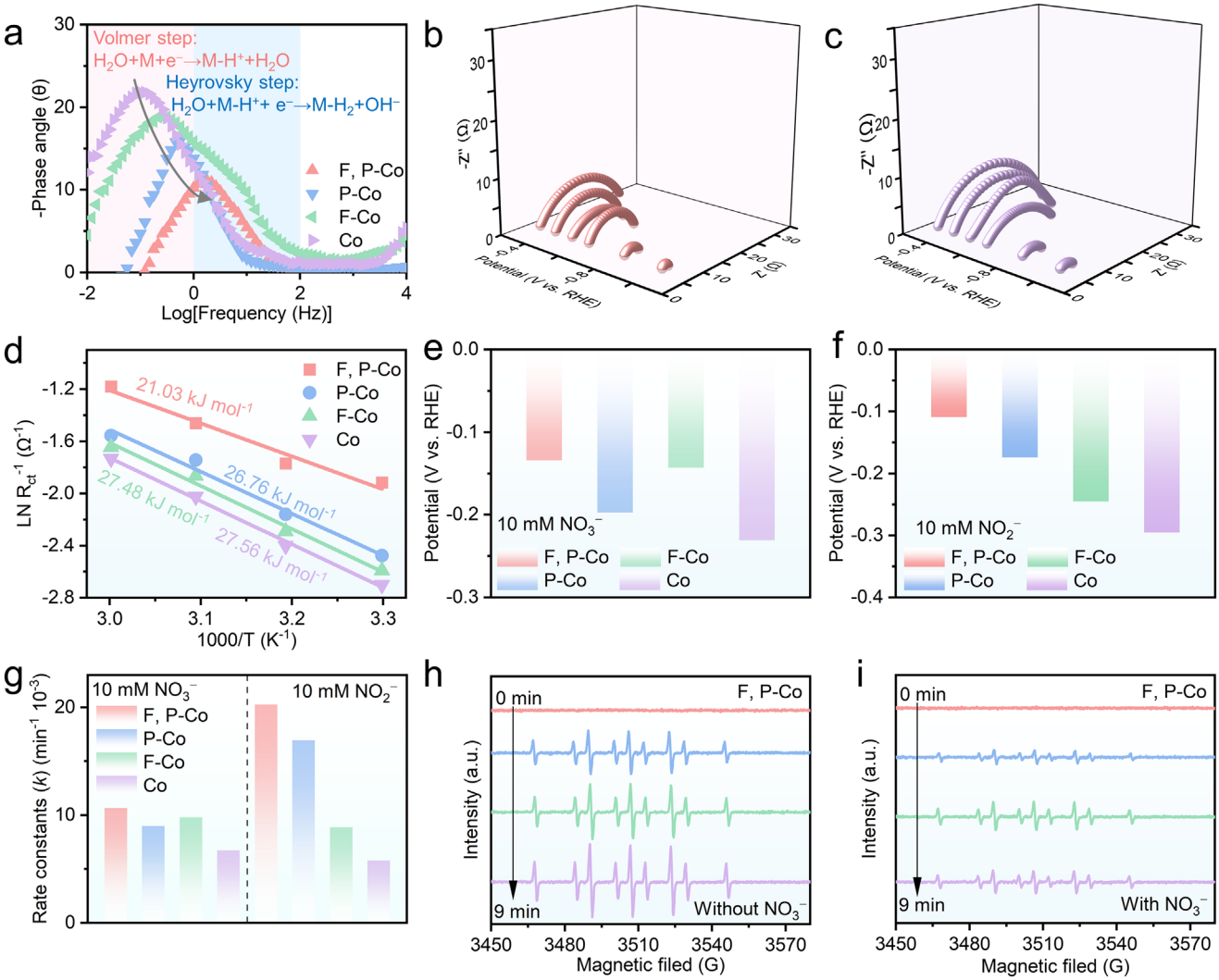

FIGURE 3 | (a) Bode phase plots of the F, P-Co, P-Co, F-Co and Co catalysts. *Operando* EIS spectra of the b) F, P-Co and c) Co. d) E_a for NO_3RR on the F, P-Co, P-Co, F-Co and Co catalysts calculated by the Arrhenius formula. The LSV-derived potentials at −5 mA cm^{-2} in e) 10 mM NO_3^- and f) NO_2^- solutions. g) The calculated reaction constants (k_1 for NO_3^--to-NO_2^- and k_2 for NO_2^--to-NH_3 conversion) for the F, P-Co, P-Co, F-Co and Co catalysts. DMPO-involved *operando* EPR spectra of F, P-Co in 0.1 M K_2SO_4 solution h) without and i) with 10 mM NO_3^-.

contrast, F-Co exhibits a lower k_2 value than F, P-Co and P-Co, underscoring the essential role of P doping in promoting the subsequent conversion of NO_2^- to NH_3. This kinetic behavior is consistent with the high FE_{NO2}^- observed for F-Co. Notably, the k_2/k_1 ratio for F, P-Co is 1.90, which is greater than those of P-Co, F-Co and Co, manifesting its superior ability to rapidly convert $*NO_2$ intermediate into NH_3 rather than allowing its accumulation or desorption (Figure S27). These kinetic results confirm a synergistic tandem mechanism enabled by dual doping: F-adjacent Co (F-Co) sites preferentially activate NO_3^- to generate NO_2^-, while the P-adjacent Co (P-Co) sites facilitate its subsequent hydrogenation to NH_3. To further elucidate the reaction pathway, we monitored the time-dependent product yields of NO_2^- and NH_3 during the initial 30 min of electrocatalysis. As shown in Figure S28, the NH_3 yield increases steadily, while the concentration of NO_2^- in the electrolyte remains negligible. This indicates that the $*NO_2$ intermediate generated on F-Co sites rapidly migrates to neighboring P-Co sites for further reduction, rather than desorbing from the catalyst surface to form NO_2^-.

To further elucidate the role of F and P dual-doping in modulating *H behavior, *operando* electron paramagnetic resonance (EPR) was performed using 5,5-dimethyl-1-pyrroline N-oxide (DMPO) as the *H trapping reagent. In the absence of NO_3^-, both P-Co and F, P-Co display stronger DMPO-H signals than F-Co and Co, indicating that P doping enhances water dissociation and favors *H production (Figure 3h,i; Figure S29). Upon introduction of NO_3^-, the DMPO—H signals for P-Co and F, P-Co diminish markedly, indicating efficient utilization of *H species for NO_3RR. Notably, the disparity of the peak intensities for F, P-Co is greater than those of P-Co, F-Co and Co, demonstrating that the F and P co-doping synergistically boost the hydrogenation process during NO_3RR. Time-resolved EPR analysis further reveals that *H signal initially accumulates on F, P-Co and is then progressively consumed as the reaction proceeds, which aligns with a sequential $2e^- + 6e^-$ transfer pathway. In contrast, the *H signals for the P-Co, F-Co and pure Co catalysts intensify continuously over the same period (Figure S30). Therefore, it is reasonable to conclude that F and P dual-doping optimally regulates the

generation and utilization of *H to drive the tandem NO_3RR process.

To gain deeper insights into the reaction mechanism, reaction intermediates were monitored by *operando* attenuated total reflection-surface-enhanced infrared absorption spectroscopy (ATR-SEIRAS). For F, P-Co, the signals of $*NO_3^-$ at 1390 cm^{-1} rises gradually as the potential increases, indicating strong adsorption of NO_3^- (Figure 4a) [62]. The bands appearing around 1290 and 1650 cm^{-1} are assigned to the deoxygenation intermediates of $*NO_2$ and *NO, respectively, implying effective NO_3^- reduction and enhanced adsorption of oxynitride intermediates [63]. Additionally, characteristic peaks for *NOH, and NH_4^+ are observed at 1522 and 1475 cm^{-1}, confirming the successful reduction of NO_3^- to NH_3 on the F, P-Co catalyst [62, 63]. The stronger stretching vibration of H_2O at 1615 cm^{-1} compared to the Co catalyst indicates the superior water dissociation ability of F, P-Co (Figure 4b) [63]. Also, the vibrations of nitrogen-containing adsorption intermediates, including $*NO_2$, *NOH, *NO, and NH_4^+, vanish on the Co catalyst, suggesting poor deoxygenation and hydrogenation capabilities, corroborating the EIS and EPR findings. Figure 4c–e displays the *operando* Raman spectra of F, P-Co, F-Co and pure Co at varied potentials from −0.3 to −1.0 V. While all catalysts exhibit a sulfate adsorption signal near 982 cm^{-1}, F, P-Co displays distinct peaks at 1048, 809 and 1635 cm^{-1}, assignable to $*NO_3^-$, $*NO_2$ and $*NH_3$, respectively, consistent with the ATR-SEIRAS observations [58]. Significantly, the band at 1502 cm^{-1}, corresponding to *NOH, is observed exclusively for F, P-Co, further confirming this intermediate in the NO_3RR pathway [58]. The absence of the *NOH signal on F-Co and pure Co suggests a sluggish protonation step from *NO to *NOH, likely due to insufficient *H generation. These findings are well aligned with the kinetics and EPR results, indicating that P-doped Co sites serve as the primary active centers for the hydrogenation steps.

Operando differential electrochemical mass spectrometry (DEMS) was subsequently employed to monitor key reaction intermediates and products during electrocatalysis at –0.5 V vs. RHE. As shown in Figure 4f, *Operando* DEMS spectrum of F, P-Co reveals characteristic m/z signals at 14, 15, 16, 17, 30, 31, which are assigned to the *N, *NH, $*NH_2$, NH_3, *NO, and *NOH intermediates, respectively. These results are in agreement with the *operando* Raman and in situ ATR-SEIRAS data, collectively confirming that the NO_3RR proceeds via the pathway: $*NO_3 \rightarrow *NO_2 \rightarrow *NO \rightarrow *NOH \rightarrow *N \rightarrow *NH \rightarrow *NH_2 \rightarrow *NH_3$.

Density functional theory (DFT) calculations were further carried out to clarify the influence of F and P doping on the enhanced reaction kinetics and to uncover the NO_3RR mechanism. After structural optimization, the most stable configurations of Co, F-Co, P-Co, and F, P-Co were obtained (Figures S31–S33). Crystal orbital Hamilton population (COHP) was first adopted to analyze the influence of F and P doping on $*NO_3$ adsorption (Figure 5a). The integrated COHP (ICOHP) of the Co—O bond in F-Co is calculated to be −2.88 eV, which is more negative than those of Co (−2.54) and P-Co (−2.56). This indicates that F doping strengthens the adsorption of $*NO_3$, whereas P doping alone has a minimal effect. F, P-Co achieves the lowest ICOHP of −3.00 eV, further confirming the strongest interaction with $*NO_3$. This result is well supported by the upshifted *d*-band center (ε_d, −3.53 eV) of F, P-Co toward the Fermi level, which reflects the synergistic electronic modulation induced by dual heteroatoms (Figure S34). Additionally, the charge density difference (CDD) plot of F, P-Co reveals that more charges are accumulated on $*NO_3$ (yellow region) compared to the other catalysts, indicating enhanced adsorption and activation (Figure 5b; Figures S35 and S36). This is substantiated by the increased Bader charge of NO_3^- from 0.70 |e| to 0.75 |e| after F and P doping. These results collectively establish that the incorporation of F and P creates an optimal electronic environment for NO_3^- adsorption and subsequent reduction.

Afterward, the reaction energies on the different catalysts were investigated to elucidate the mechanistic impact of F and P doping on the NO_3RR pathways. The Gibbs free energy profiles reveal distinct mechanistic behaviors. Although the Co, F-Co, and P-Co catalysts all follow a conventional direct pathway involving $*NO_3$, $*NO_2$, ($*NO_2H$), *NO, *NOH, *N, *NH, $*NH_2$, and $*NH_3$ intermediates, their kinetic bottlenecks differ significantly (Figure 5c; Figures S37–S40). For Co, the hydrogenation step of *NO to *NOH is the potential-determining step (PDS), which requires a high energy barrier of 1.58 eV (Figure 5e). In contrast, the barrier on F-Co declines to 1.12 eV, indicating that F doping is beneficial for NO_3^- reduction. Notably, P doping enables the spontaneous transformation of *NO to *NOH, shifting the PDS to NH_3 desorption with a much lower Gibbs free energy change of 0.67 eV. This is in accordance with the enhanced hydrogenation kinetics on P-Co. In contrast to the Co, F-Co, and P-Co catalysts, F, P-Co exhibits a unique mechanism involving $*NO_2$ spillover from the F-Co site to the P-Co site. This spillover is driven by its more favorable energetics compared to the direct hydrogenation of $*NO_2$ to $*NO_2H$) (Figure 5d; Figure S41). Moreover, the $*NO_2$ spillover process is thermodynamically preferred over $*NO_2$ desorption, further supporting the proposed spillover mechanism (Figure S42). This was further validated by the more negative ICOHP for the P-Co site, indicating the stronger interaction with $*NO_2$ intermediates compared to the F-Co site (Figure 5f,g). This thermodynamically favorable $*NO_2$ spillover process thus enables rapid *NO-to-*NOH conversion. Additionally, the lowest energy uphill of just 0.09 eV for PDS is achieved with the F, P-Co catalyst, which verifies the critical role of F and P dual doping in promoting NO_3^- reduction and $*NH_3$ desorption, thus contributing to the supreme intrinsic activity for NH_3 electrosynthesis. To further understand the role of hydrogenation dynamics in the enhanced $*NO_2$ spillover mechanism, the water dissociation processes were also calculated. Unlike the high energy barrier for H_2O dissociation on Co and F-Co sites, this process occurs readily on P-Co sites, facilitating the generation of *H species. This computational insight accounts for the enhanced hydrogenation kinetics and improved NH_3 selectivity observed experimentally for the NO_3RR (Figure 5h).

Integrating these findings, we propose an atomically tandem mechanism to describe the NO_3RR pathway on the F, P-Co catalyst, as illustrated in Figure 5i. This process initiates with preferential adsorption and activation of NO_3^- at F-Co sites, where efficient deoxygenation generates a high local concentration of $*NO_2$ intermediates. Through the $*NO_2$ spillover process, the generated $*NO_2$ can spontaneously transfer from F-Co sites to P-Co sites, which serve as dedicated hydrogenation centers. This spatial decoupling is further enhanced by two key properties of the P-Co sites: (i) their exceptional ability to facilitate H_2O dissociation, ensuring an adequate supply of *H, and (ii) the

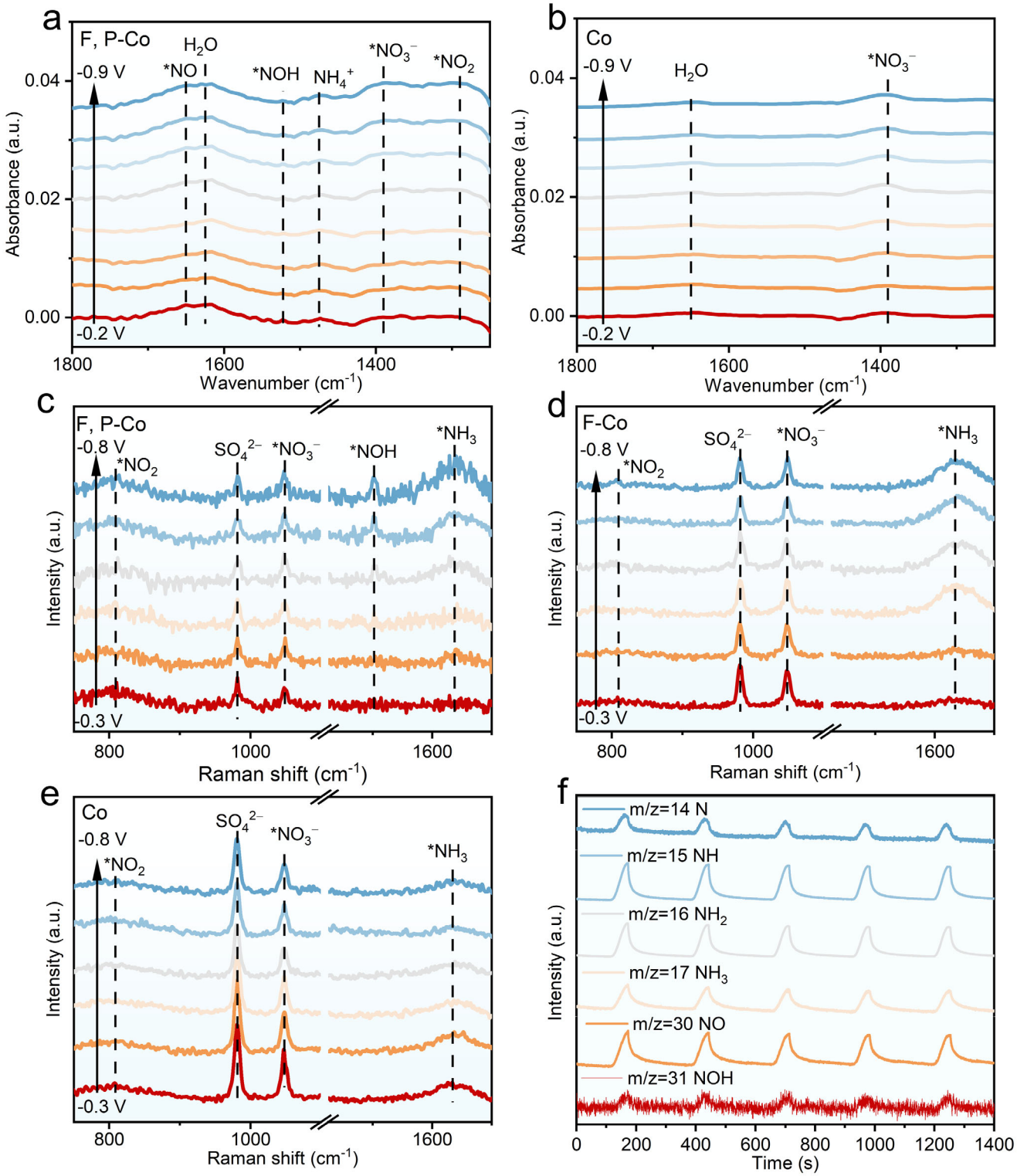

FIGURE 4 | *Operando* ATR-SEIRAS spectra of a) F, P-Co and b) Co with the change of potential. *Operando* Raman spectra of NO_3RR on c) F, P-Co, d) F-Co, and e) Co with the change of potential. f) *Operando* DEMS spectra of NO_3RR on F, P-Co.

reduced hydrogenation energy on the P-Co sites, thus facilitating *H capture by nitrogen-containing intermediates. This synergy establishes an efficient tandem process within F, P-Co: F-Co sites activate NO_3^-, while adjacent P-Co sites facilitate hydrogenation, collectively boosting both the activity and selectivity of the NO_3RR toward NH_3.

Building on the impressive electrocatalytic performance of the F, P-Co catalyst for the NO_3RR, we investigated its potential application in struvite synthesis. Using a simple co-precipitation approach, high-purity struvite with an impressive NH_3 recovery rate of 87.7% was obtained, implying its promise for converting sewage to valuable struvite (Figure 6a,b; Figure S43). To

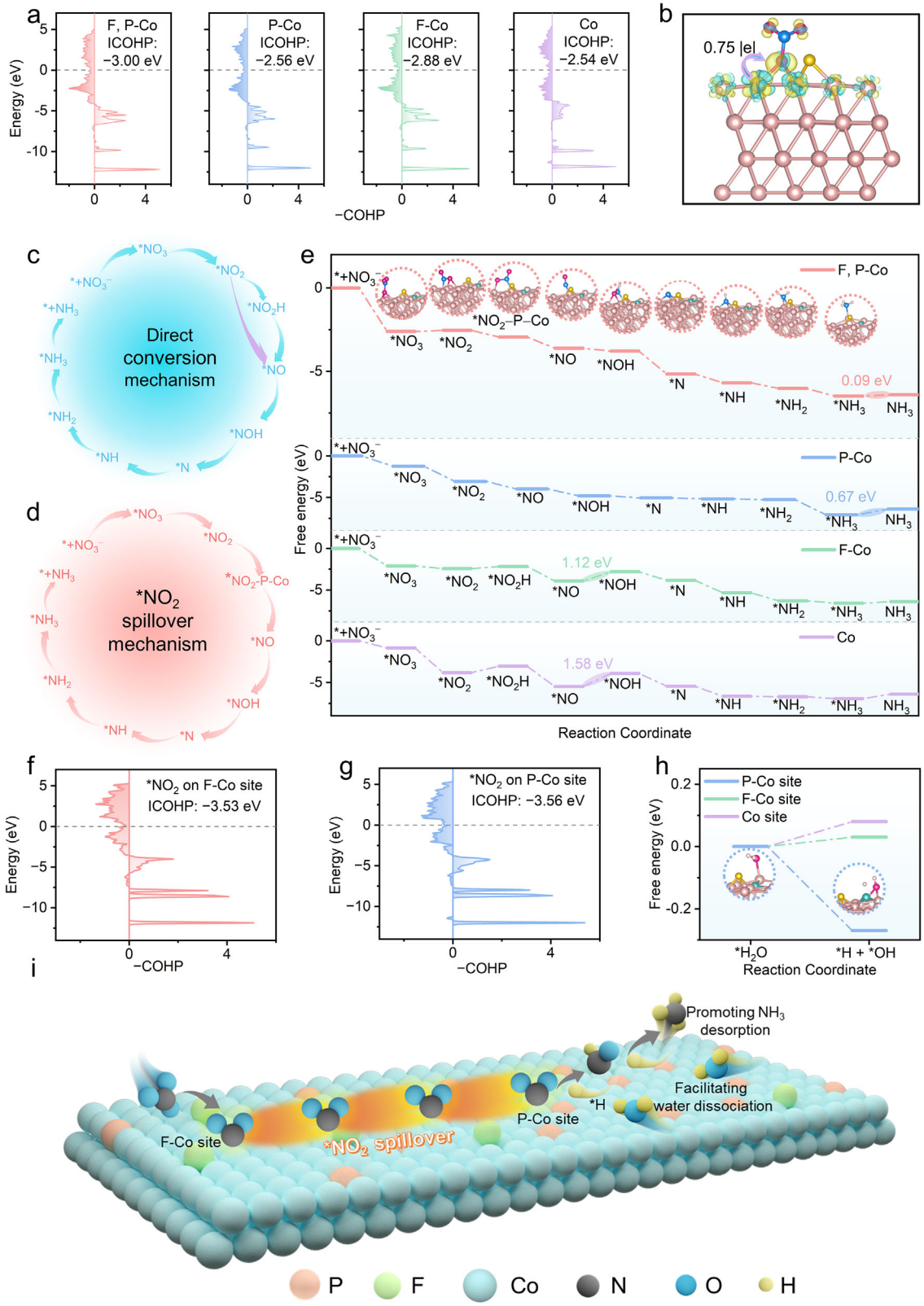

FIGURE 5 | Mechanistic exploration based on DFT calculations. a) COHP analyses of Co—O bond after $*NO_3$ adsorbed on the F, P-Co, P-Co, F-Co, and Co catalysts. b) The CDD plot of F, P-Co. Schematic illustrations of the NO_3RR pathways of c) direct conversion mechanism and d) $*NO_2$ spillover mechanism. e) The calculated Gibbs free energy diagrams for NO_3RR on the F, P-Co, P-Co, F-Co, and Co catalysts, with the optimized structures of NO_3RR intermediates on F, P-Co. Crystal orbital Hamilton population (COHP) analysis of Co—O bond + Co—N bond with $*NO_2$ adsorbed on the f) F-Co site and g) P-Co site of F, P-Co. h) The calculated Gibbs free energy diagrams for water dissociation on F-Co, P-Co, and Co sites of F, P-Co. i) Schematic illustration of the atomically tandem mechanism via $*NO_2$ spillover on the F, P-Co catalyst.

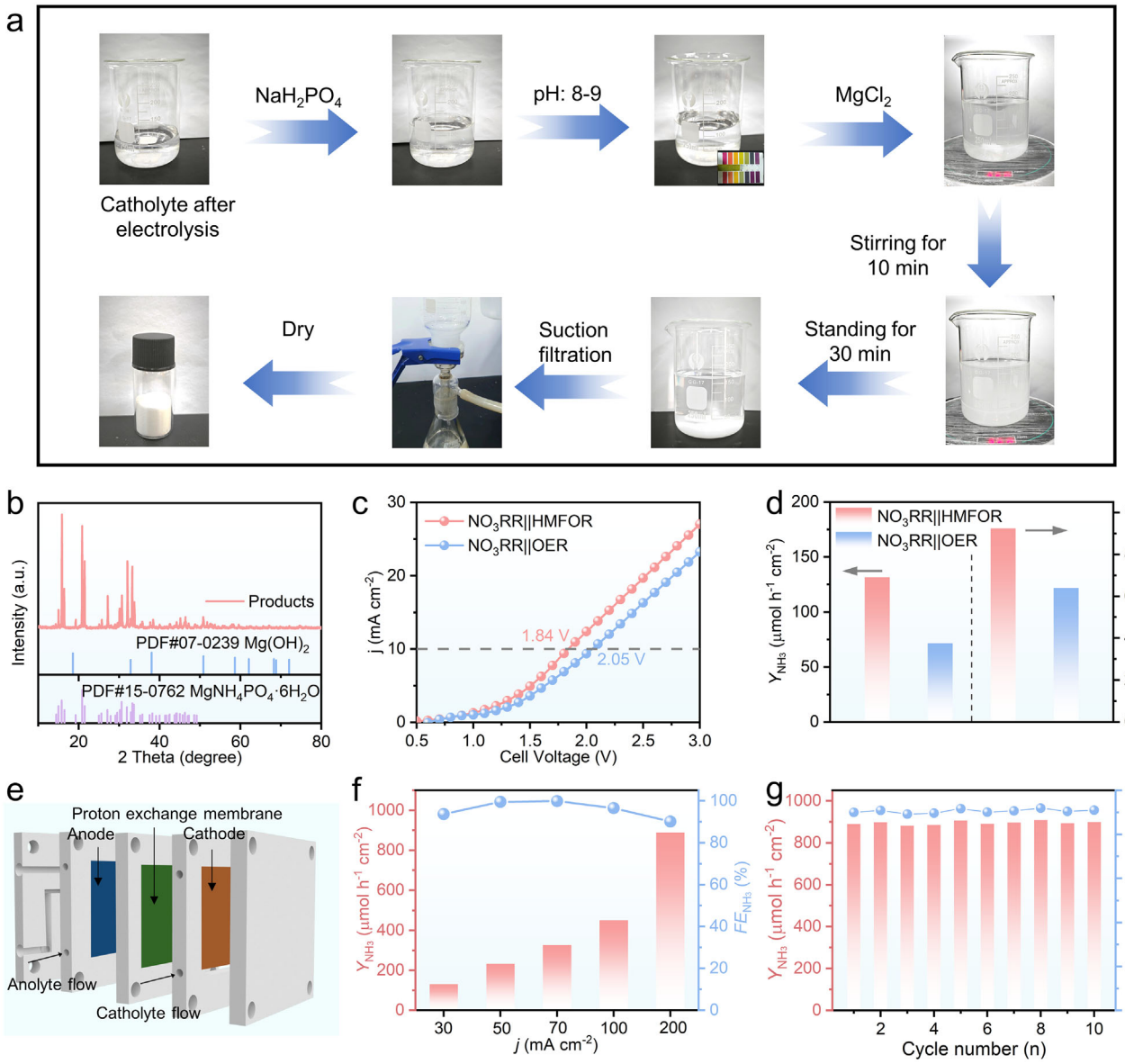

FIGURE 6 | Applications. a) Photos of the synthetic process of struvite. b) XRD patterns of the as-synthesized struvite. c) LSV curves with the NO_3RR//OER and NO_3RR//HMFOR electrolyzers. d) Y_{NH3} and FE_{NH3} with the F, P-Co-based NO_3RR//OER and NO_3RR//HMFOR electrolyzers at 2 V. e) Schematic diagram of the NO_3RR//HMFOR flow cells. f) Y_{NH3} and FE_{NH3} at different current densities in flow cells with 10 mM KNO_3. g) Stability test at 200 mA cm^{-2}.

demonstrate the feasibility of coupling biomass upgrading with NH_3 electrosynthesis, the anodic oxygen evolution reaction (OER) was replaced by HMF oxidation reaction (HMFOR) using F, P-Co as a bifunctional catalyst (Figure S44). 0.1 M K_2SO_4 + 10 mM KNO_3 was employed as the catholyte, and 0.1 M KOH + 10 mM HMF was used as the anolyte for this system. As depicted in Figure 6c, compared to the NO_3RR||OER system, a notable reduction of 210 mV was observed with the addition of HMF, requiring a low voltage of 1.84 V to deliver a current density of 10 mA cm^{-2}. The Y_{NH3} and FE_{NH3} reach 131.8 μmol h^{-1} cm^{-2} and 92.3% in the NO_3RR||HMFOR device at 2 V, respectively, indicating an enhanced catalytic efficiency (Figure 6d). This improvement stems from the faster reaction rates of HMFOR compared to OER. Meanwhile, a distinguished Y_{NH3} of 889.5 μmol h^{-1} cm^{-2}, with a high FE_{NH3} of 90.1% and excellent durability for 10 cycles is achieved in a flow cell at a large current density of 200 mA cm^{-2}, highlighting its advantages in mass production of NH_3 (Figure 6e–g) The Y_{NH3} surpasses most results of the state-of-the-art coupled NO_3RR systems (Table S4). Simultaneously, HMF was oxidized to 2,5-furandicarboxylic acid (FDCA) at the anode, as verified by the ^1H NMR spectroscopy (Figure S45) [64, 65]. These results underscore the high potential of the F, P-Co catalyst for the simultaneous electrosynthesis of NH_3 and value-added chemicals.

3 | Conclusion

In summary, we have developed an atomically tandem F, P-Co catalyst for efficient electroreduction of dilute NO_3^- to NH_3 under neutral conditions. The F, P-Co catalyst demonstrates exceptional performance, achieving a high Y_{NH3} of 357.5 μmol

h^{-1} cm^{-2} and a FE_{NH3} of 96.0% at a low potential of −0.5 V vs. RHE. It also exhibits remarkable stability, maintaining robust activity for 200 h in a 10 mM NO_3^- solution, thereby surpassing most state-of-the-art catalysts for neutral NO_3RR. Furthermore, the as-prepared catalyst demonstrates great practical potential, achieving an NH_3 yield rate of 889.5 μmol h^{-1} cm^{-2} at an industrial current density of 200 mA cm^{-2} in a flow cell system coupled with the oxidative upgrading of HMFOR. The atomic-scale relay catalytic mechanism was unequivocally substantiated through theoretical calculations combined with comprehensive kinetic analyses, *operando* EPR, *operando* Raman, and *operando* ATR-SEIRAS. This multi-faceted approach confirms that F-Co sites preferentially adsorb and reduce NO_3^- to $*NO_2$, which then spontaneously migrates to adjacent P-Co sites for efficient hydrogenation. The P-Co site enhances water dissociation, which greatly promotes *H generation and thereby accelerates the hydrogenation kinetics for the $*NO_2$-to-NH_3 conversion. This work provides profound atomic-level insight into tandem catalysis for the NO_3RR through controlled intermediate spillover and establishes a practical and efficient pathway for large-scale electrochemical NH_3 synthesis.

Acknowledgements

This work was financially supported by the National Natural Science Foundation of China (22272150 and 22302177), the Key Science and Technology Project of Jinhua City (2024-1-004), and the Self Designed Scientific Research of Zhejiang Normal University (2021ZS0604), the Scientific Research Fund of Zhejiang Provincial Education Department (Y202457290), and Jinhua Science and Technology Plan Project (2024-4-021). The authors thank Dr. Leijie Zhang (Specreation Instruments Co., Ltd.) for his assistance for XAFS characterization.

Conflicts of Interest

The authors declare no conflicts of interest.

Data Availability Statement

Research data are not shared.

References

1. W. Guo, K. Zhang, Z. Liang, R. Zou, and Q. Xu, "Electrochemical Nitrogen Fixation and Utilization: Theories, Advanced Catalyst Materials and System Design," *Chemical Society Reviews* 48 (2019): 5658–5716, https://doi.org/10.1039/C9CS00159J.

2. J. G. Chen, R. M. Crooks, L. C. Seefeldt, et al., "Beyond Fossil Fuel–Driven Nitrogen Transformations," *Science* 360 (2018): aar6611, https://doi.org/10.1126/science.aar6611.

3. H. Xu, Y. Ma, J. Chen, W.-X. Zhang, and J. Yang, "Electrocatalytic Reduction Of Nitrate—A Step Towards a Sustainable Nitrogen Cycle," *Chemical Society Reviews* 51 (2022): 2710–2758, https://doi.org/10.1039/D1CS00857A.

4. J. Theerthagiri, J. Park, H. T. Das, et al., "Electrocatalytic Conversion of Nitrate Waste Into Ammonia: A Review," *Environmental Chemistry Letters* 20 (2022): 2929–2949, https://doi.org/10.1007/s10311-022-01469-y.

5. S. Han, H. Li, T. Li, et al., "Ultralow Overpotential Nitrate Reduction to Ammonia via A Three-Step Relay Mechanism," *Nature Catalysis* 6 (2023): 402–414, https://doi.org/10.1038/s41929-023-00951-2.

6. J. W. Erisman, M. A. Sutton, J. Galloway, Z. Klimont, and W. Winiwarter, "How a Century of Ammonia Synthesis Changed the World," *Nature Geoscience* 1 (2008): 636–639, https://doi.org/10.1038/ngeo325.

7. C. H. Christensen, T. Johannessen, R. Z. Sørensen, and J. K. Nørskov, "Towards An Ammonia-Mediated Hydrogen Economy?," *Catalysis Today* 111 (2006): 140–144, https://doi.org/10.1016/j.cattod.2005.10.011.

8. K. Zhang, A. Cao, L. H. Wandall, et al., "Spin-Mediated Promotion of Co Catalysts for Ammonia Synthesis," *Science* 383 (2024): 1357–1363, https://doi.org/10.1126/science.adn0558.

9. H. Wang, Y. Chen, R. Fan, et al., "Selective Electrochemical Reduction of Nitrogen to Ammonia by Adjusting the Three-Phase Interface," *Research* 2019 (2019): 1401209.

10. H. Zhang, K. Fang, J. Yang, et al., "Strategies and Applications of Electrocatalytic Nitrate Reduction Towards Ammonia," *Coordination Chemistry Reviews* 506 (2024): 215723, https://doi.org/10.1016/j.ccr.2024.215723.

11. J. Liang, Z. Li, L. Zhang, et al., "Advances in Ammonia Electrosynthesis From Ambient Nitrate/Nitrite Reduction," *Chemistry* 9 (2023): 1768–1827, https://doi.org/10.1016/j.chempr.2023.05.037.

12. Y. Wang, C. Wang, M. Li, Y. Yu, and B. Zhang, "Nitrate Electroreduction: Mechanism Insight, In Situ Characterization, Performance Evaluation, and Challenges," *Chemical Society Reviews* 50 (2021): 6720–6733, https://doi.org/10.1039/D1CS00116G.

13. Y. Xiong, Y. Wang, J. Zhou, F. Liu, F. Hao, and Z. Fan, "Electrochemical Nitrate Reduction: Ammonia Synthesis and the Beyond," *Advanced Materials* 36 (2024): 2304021, https://doi.org/10.1002/adma.202304021.

14. Y. Zhu, H. Duan, C. G. Gruber, et al., "Boosting Electrocatalytic Nitrate Reduction Through Enhanced Mass Transfer in Cu-Bipyridine 2D Covalent Organic Framework Films," *Angewandte Chemie International Edition* 64 (2025): 202421821, https://doi.org/10.1002/anie.202421821.

15. Y. Wang, H. Li, W. Zhou, X. Zhang, B. Zhang, and Y. Yu, "Structurally Disordered RuO_2 Nanosheets With Rich Oxygen Vacancies for Enhanced Nitrate Electroreduction to Ammonia," *Angewandte Chemie International Edition* 61 (2022): 202202604, https://doi.org/10.1002/anie.202202604.

16. Y. Wang, W. Zhou, R. Jia, Y. Yu, and B. Zhang, "Unveiling the Activity Origin of a Copper-Based Electrocatalyst for Selective Nitrate Reduction to Ammonia," *Angewandte Chemie International Edition* 59 (2020): 5350, https://doi.org/10.1002/anie.201915992.

17. Z. Y. Wu, M. Karamad, X. Yong, et al., "Electrochemical Ammonia Synthesis via Nitrate Reduction on Fe Single Atom Catalyst," *Nature Communications* 12 (2021): 2870.

18. H. Zhang, H. Wang, X. Cao, et al., "Unveiling Cutting-Edge Developments in Electrocatalytic Nitrate-to-Ammonia Conversion," *Advanced Materials* 36 (2024): 2312746, https://doi.org/10.1002/adma.202312746.

19. Y. Wang, A. Xu, Z. Wang, et al., "Enhanced Nitrate-to-Ammonia Activity on Copper–Nickel Alloys via Tuning of Intermediate Adsorption," *Journal of the American Chemical Society* 142 (2020): 5702–5708, https://doi.org/10.1021/jacs.9b13347.

20. G. F. Chen, Y. Yuan, H. Jiang, et al., "Electrochemical Reduction of Nitrate to Ammonia via Direct Eight-Electron Transfer using a Copper–Molecular Solid Catalyst," *Nature Energy* 5 (2020): 605–613, https://doi.org/10.1038/s41560-020-0654-1.

21. J. Zhou, M. Wen, R. Huang, et al., "Regulating Active Hydrogen Adsorbed on Grain Boundary Defects of Nano-Nickel for Boosting Ammonia Electrosynthesis From Nitrate," *Energy & Environmental Science* 16 (2023): 2611–2620, https://doi.org/10.1039/D2EE04095F.

22. K. Fan, W. Xie, J. Li, et al., "Active Hydrogen Boosts Electrochemical Nitrate Reduction to Ammonia," *Nature Communications* 13 (2022): 7958, https://doi.org/10.1038/s41467-022-35664-w.

23. Y. Lv, S. W. Ke, Y. Gu, et al., "Highly Efficient Electrochemical Nitrate Reduction to Ammonia in Strong Acid Conditions With Fe2

M-Trinuclear-Cluster Metal–Organic Frameworks," *Angewandte Chemie International Edition* 62 (2023): 202305246, https://doi.org/10.1002/anie.202305246.

24. B. Kang, B. Xu, Z. Chen, F. Li, and Y. Wang, "Promoting Active Hydrogen Supply For Kinetically Matched Tandem Electrocatalytic Nitrate Reduction To Ammonia," *Applied Catalysis B: Environment and Energy* 360 (2025): 124528.

25. W. Ye, Y. Yao, X. Wei, et al., "Continuous Intermediates Spillover Boosts Electrochemical Nitrate Conversion to Ammonia Over Dual Single-Atom Alloy," *Angewandte Chemie International Edition* 64 (2025): 202509303, https://doi.org/10.1002/anie.202509303.

26. P. H. van Langevelde, I. Katsounaros, and M. T. M. Koper, "Electrocatalytic Nitrate Reduction for Sustainable Ammonia Production," *Joule* 5 (2021): 290–294, https://doi.org/10.1016/j.joule.2020.12.025.

27. F. Y. Chen, Z. Y. Wu, S. Gupta, et al., "Efficient Conversion of Low-Concentration Nitrate Sources Into Ammonia on a Ru-Dispersed Cu Nanowire Electrocatalyst," *Nature Nanotechnology* 17 (2022): 759–767, https://doi.org/10.1038/s41565-022-01121-4.

28. W. J. Sun, H. Q. Ji, L. X. Li, et al., "Built-in Electric Field Triggered Interfacial Accumulation Effect for Efficient Nitrate Removal at Ultra-Low Concentration and Electroreduction to Ammonia," *Angewandte Chemie International Edition* 60 (2021): 22933, https://doi.org/10.1002/anie.202109785.

29. Q. Song, M. Li, X. Hou, et al., "Anchored Fe Atoms for N=O Bond Activation to Boost Electrocatalytic Nitrate Reduction at Low Concentrations," *Applied Catalysis B: Environmental* 317 (2022): 121721, https://doi.org/10.1016/j.apcatb.2022.121721.

30. H. Zhang, J. Ran, Y. Ding, et al., "In Situ Manipulation of Interfacial Water in Ni-Co3O4 for Efficient Neutral Nitrate Electroreduction to Ammonia," *Applied Catalysis B: Environment and Energy* 381 (2026): 125830, https://doi.org/10.1016/j.apcatb.2025.125830.

31. S. Liang, X. Teng, H. Xu, L. Chen, and J. Shi, "H* Species Regulation by Mn-Co(OH) 2 for Efficient Nitrate Electro-Reduction in Neutral Solution," *Angewandte Chemie International Edition* 63 (2024): 202400206, https://doi.org/10.1002/anie.202400206.

32. H. Fu, S. Lu, Y. Xin, et al., "In Situ Bulk Hydrogen Intercalation in a Mirror-Symmetric Ru/WO_{3-x} Nanoarray Boosts Neutral Electrocatalytic Nitrate Reduction to Ammonia," *Energy & Environmental Science* 18 (2025): 818–830, https://doi.org/10.1039/D4EE03970J.

33. P. B. O'Mara, P. Wilde, T. M. Benedetti, et al., "Cascade Reactions in Nanozymes: Spatially Separated Active Sites inside Ag-Core–Porous-Cu-Shell Nanoparticles for Multistep Carbon Dioxide Reduction to Higher Organic Molecules," *Journal of the American Chemical Society* 141 (2019): 14093–14097.

34. R. Cao, R. Thapa, H. Kim, et al., "Promotion of Oxygen Reduction by a Bio-Inspired Tethered Iron Phthalocyanine Carbon Nanotube-Based Catalyst," *Nature Communications* 4 (2013): 2076, https://doi.org/10.1038/ncomms3076.

35. H. Cai, H. Yang, D. Li, et al., "Combining the Active Site Construction and Microenvironment Regulation via a Bio-Inspired Strategy Boosts CO 2 Electroreduction Under Ampere-Level Current Densities," *Angewandte Chemie International Edition* 64 (2025): 202425325, https://doi.org/10.1002/anie.202425325.

36. D. Grumelli, B. Wurster, S. Stepanow, and K. Kern, "Bio-Inspired Nanocatalysts for the Oxygen Reduction Reaction," *Nature Communications* 4 (2013): 2904, https://doi.org/10.1038/ncomms3904.

37. X. Jiang, J. Li, B. Yang, et al., "A Bio-Inspired Cu 4 O 4 Cubane: Effective Molecular Catalysts for Electrocatalytic Water Oxidation in Aqueous Solution," *Angewandte Chemie International Edition* 57 (2018): 7850, https://doi.org/10.1002/anie.201803944.

38. J. Wang, T. Feng, J. Chen, et al., "Electrocatalytic Nitrate/Nitrite Reduction to Ammonia Synthesis Using Metal Nanocatalysts and Bio-Inspired Metalloenzymes," *Nano Energy* 86 (2021): 106088.

39. D. G. Boucher, E. Carroll, Z. A. Nguyen, et al., "Bioelectrocatalytic Synthesis: Concepts and Applications," *Angewandte Chemie International Edition* 62 (2023): 202307780, https://doi.org/10.1002/anie.202307780.

40. R. D. Milton and S. D. Minteer, "Enzymatic Bioelectrosynthetic Ammonia Production: Recent Electrochemistry of Nitrogenase, Nitrate Reductase, and Nitrite Reductase," *ChemPlusChem* 82 (2017): 513–521, https://doi.org/10.1002/cplu.201600442.

41. E. Murphy, Y. Liu, I. Matanovic, et al., "Elucidating Electrochemical Nitrate and Nitrite Reduction Over Atomically-Dispersed Transition Metal Sites," *Nature Communications* 14 (2023): 4554, https://doi.org/10.1038/s41467-023-40174-4.

42. X. Shi, M. Xie, K. Yang, et al., "Synergistic Effect of Ni/Ni(OH) 2 Core-Shell Catalyst Boosts Tandem Nitrate Reduction for Ampere-Level Ammonia Production," *Angewandte Chemie International Edition* 63 (2024): 202406750, https://doi.org/10.1002/anie.202406750.

43. L. Liu, S. J. Zheng, H. Chen, J. Cai, and S. Q. Zang, "Tandem Nitrate-to-Ammonia Conversion on Atomically Precise Silver Nanocluster/MXene Electrocatalyst," *Angewandte Chemie International Edition* 63 (2024): 202316910, https://doi.org/10.1002/anie.202316910.

44. H. Jiang, G. F. Chen, O. Savateev, et al., "Enabled Efficient Ammonia Synthesis and Energy Supply in a Zinc–Nitrate Battery System by Separating Nitrate Reduction Process Into Two Stages," *Angewandte Chemie International Edition* 62 (2023): 202218717, https://doi.org/10.1002/anie.202218717.

45. W. He, J. Zhang, S. Dieckhöfer, et al., "Splicing the Active Phases of Copper/Cobalt-Based Catalysts Achieves High-Rate Tandem Electroreduction of Nitrate to Ammonia," *Nature Communications* 13 (2022): 1129, https://doi.org/10.1038/s41467-022-28728-4.

46. Y. Liu, J. Wei, Z. Yang, et al., "Efficient Tandem Electroreduction of Nitrate Into Ammonia Through Coupling Cu Single Atoms With Adjacent Co3O4," *Nature Communications* 15 (2024): 3619, https://doi.org/10.1038/s41467-024-48035-4.

47. C. Guan, A. Sumboja, W. Zang, et al., "Decorating Co/CoNx Nanoparticles in Nitrogen-Doped Carbon Nanoarrays for Flexible and Rechargeable Zinc-Air Batteries," *Energy Storage Materials* 16 (2019): 243–250, https://doi.org/10.1016/j.ensm.2018.06.001.

48. J. Y. Fang, Q. Z. Zheng, Y. Y. Lou, et al., "Ampere-Level Current Density Ammonia Electrochemical Synthesis Using CuCo Nanosheets Simulating Nitrite Reductase Bifunctional Nature," *Nature Communications* 13 (2022): 7899, https://doi.org/10.1038/s41467-022-35533-6.

49. K. Xu, Y. Sun, X. Li, et al., "Fluorine-Induced Dual Defects in Cobalt Phosphide Nanosheets Enhance Hydrogen Evolution Reaction Activity," *ACS Materials Letters* 2 (2020): 736–743, https://doi.org/10.1021/acsmaterialslett.0c00209.

50. X. Chen, M. Wei, and J. Zhou, "Fluorine-Doping-Assisted Vacancy Engineering for Efficient Electrocatalyst Toward Hydrogen Production," *Journal of Materials Chemistry A* 9 (2021): 22626–22634, https://doi.org/10.1039/D1TA05946G.

51. E. Cao, Z. Chen, H. Wu, et al., "Boron-Induced Electronic-Structure Reformation of CoP Nanoparticles Drives Enhanced pH-Universal Hydrogen Evolution," *Angewandte Chemie International Edition* 59 (2020): 4154–4160, https://doi.org/10.1002/anie.201915254.

52. X. Li, Y. Sun, L. Zhou, et al., "Suppressing Jahn–Teller Distortion and Locking Lattice Water With Doped Fe(iii) in Birnessite Toward Fast and Stable Zinc-Ion Batteries," *Materials Horizons* 11 (2024): 4133–4143, https://doi.org/10.1039/D4MH00544A.

53. S. Y. Wang, X. Ji, S. C. Wang, et al., "Stabilization of Electron-Deficient Cu 1δ+ Species by Cl–Doped CeO_2 Constructed via Electrochemical Reconstruction for Electroreduction of Nitrate to Ammonia Over 2500 H," *Advanced Functional Materials* 35 (2025): 2502073, https://doi.org/10.1002/adfm.202502073.

54. Y. Li, C. Wang, L. Yang, et al., "Enhancement of Nitrate-to-Ammonia on Amorphous CeO_x -Modified Cu via Tuning of Active Hydrogen

Supply," *Advanced Energy Materials* 14 (2024): 2303863, https://doi.org/10.1002/aenm.202303863.

55. L. Sun and B. Liu, "Mesoporous PdN Alloy Nanocubes for Efficient Electrochemical Nitrate Reduction to Ammonia," *Advanced Materials* 35 (2023): 2207305, https://doi.org/10.1002/adma.202207305.

56. H. Du, H. Guo, K. Wang, et al., "Durable Electrocatalytic Reduction of Nitrate to Ammonia Over Defective Pseudobrookite Fe_2 TiO_5 Nanofibers With Abundant Oxygen Vacancies," *Angewandte Chemie International Edition* 62 (2023): 202215782, https://doi.org/10.1002/anie.202215782.

57. D. Chen, S. Zhang, D. Yin, et al., "Tailored p-Orbital Delocalization by Diatomic Pt-Ce Induced Interlayer Spacing Engineering for Highly-Efficient Ammonia Electrosynthesis," *Advanced Energy Materials* 13 (2023): 2203201, https://doi.org/10.1002/aenm.202203201.

58. R. Zhao, Q. Yan, L. Yu, et al., "A Bi-Co Corridor Construction Effectively Improving the Selectivity of Electrocatalytic Nitrate Reduction Toward Ammonia by Nearly 100%," *Advanced Materials* 35 (2023): 2306633, https://doi.org/10.1002/adma.202306633.

59. G. Zhang, X. Li, K. Chen, Y. Guo, D. Ma, and K. Chu, "Tandem Electrocatalytic Nitrate Reduction to Ammonia on MBenes," *Angewandte Chemie International Edition* 62 (2023): 202300054, https://doi.org/10.1002/anie.202300054.

60. L. Wu, J. Feng, L. Zhang, et al., "Boosting Electrocatalytic Nitrate-to-Ammonia via Tuning of N-Intermediate Adsorption on a Zn−Cu Catalyst," *Angewandte Chemie International Edition* 62 (2023): 202307952, https://doi.org/10.1002/anie.202307952.

61. Z. Fan, C. Cao, X. Yang, et al., "Interfacial Electronic Interactions Promoted Activation for Nitrate Electroreduction to Ammonia Over Ag-Modified Co_3O_4," *Angewandte Chemie International Edition* 63 (2024): 202410356, https://doi.org/10.1002/anie.202410356.

62. W. Liu, J. Chen, Y. Wei, et al., "Regulating Local Electron Distribution of Cu Electrocatalyst via Boron Doping for Boosting Rapid Absorption and Conversion of Nitrate to Ammonia," *Advanced Functional Materials* 34 (2024): 2408732, https://doi.org/10.1002/adfm.202408732.

63. L. Yang, C. Wang, Y. Li, et al., "Frustrated Lewis Pairs on Zr Single Atoms Supported N-Doped TiO_{2-X} Catalysts for Electrochemical Nitrate Reduction To Ammonia," *Advanced Functional Materials* 34 (2024): 2401094, https://doi.org/10.1002/adfm.202401094.

64. X. Liu, Y. Luo, H. Ma, et al., "Hydrogen-Binding-Initiated Activation of O−H Bonds on a Nitrogen-Doped Surface for the Catalytic Oxidation of Biomass Hydroxyl Compounds," *Angewandte Chemie International Edition* 60 (2021): 18103, https://doi.org/10.1002/anie.202103604.

65. J. Lei, H. Zhang, J. Yang, et al., "Structural designs and mechanism insights Into electrocatalytic oxidation of 5-hydroxymethylfurfural," *Journal of Energy Chemistry* 100 (2025): 792–814, https://doi.org/10.1016/j.jechem.2024.08.066.

Supporting Information

Additional supporting information can be found online in the Supporting Information section.

Supporting file: aenm70469-sup-0001-SuppMat.docx